



# Reconstruction and Analysis of Thermodynamically Constrained Models Reveal Metabolic Responses of a Deep-Sea Bacterium to Temperature Perturbations

Keith Dufault-Thompson,<sup>a,\*</sup> Chang Nie,<sup>b</sup> Huahua Jian,<sup>b</sup>  Fengping Wang,<sup>b,c</sup>  Ying Zhang<sup>a</sup>

<sup>a</sup>Department of Cell and Molecular Biology, College of the Environment and Life Sciences, University of Rhode Island, Kingston, Rhode Island, USA

<sup>b</sup>State Key Laboratory of Microbial Metabolism, Joint International Research Laboratory of Metabolic & Development Sciences, School of Life Sciences and Biotechnology, Shanghai Jiao Tong University, Shanghai, People's Republic of China

<sup>c</sup>School of Oceanography, Shanghai JiaoTong University, Shanghai, People's Republic of China

**ABSTRACT** Microbial acclimation to different temperature conditions can involve broad changes in cell composition and metabolic efficiency. A systems-level view of these metabolic responses in nonmesophilic organisms, however, is currently missing. In this study, thermodynamically constrained genome-scale models were applied to simulate the metabolic responses of a deep-sea psychrophilic bacterium, *Shewanella psychrophila* WP2, under suboptimal (4°C), optimal (15°C), and supraoptimal (20°C) growth temperatures. The models were calibrated with experimentally determined growth rates of WP2. Gibbs free energy change of reactions ( $\Delta_r G'$ ), metabolic fluxes, and metabolite concentrations were predicted using random simulations to characterize temperature-dependent changes in the metabolism. The modeling revealed the highest metabolic efficiency at the optimal temperature, and it suggested distinct patterns of ATP production and consumption that could lead to lower metabolic efficiency under suboptimal or supraoptimal temperatures. The modeling also predicted rearrangement of fluxes through multiple metabolic pathways, including the glycolysis pathway, Entner-Doudoroff pathway, tricarboxylic acid (TCA) cycle, and electron transport system, and these predictions were corroborated through comparisons to WP2 transcriptomes. Furthermore, predictions of metabolite concentrations revealed the potential conservation of reducing equivalents and ATP in the suboptimal temperature, consistent with experimental observations from other psychrophiles. Taken together, the WP2 models provided mechanistic insights into the metabolism of a psychrophile in response to different temperatures.

**IMPORTANCE** Metabolic flexibility is a central component of any organism's ability to survive and adapt to changes in environmental conditions. This study represents the first application of thermodynamically constrained genome-scale models in simulating the metabolic responses of a deep-sea psychrophilic bacterium to various temperatures. The models predicted differences in metabolic efficiency that were attributed to changes in metabolic pathway utilization and metabolite concentration during growth under optimal and nonoptimal temperatures. Experimental growth measurements were used for model calibration, and temperature-dependent transcriptomic changes corroborated the model-predicted rearrangement of metabolic fluxes. Overall, this study highlights the utility of modeling approaches in studying the temperature-driven metabolic responses of an extremophilic organism.

**KEYWORDS** deep-sea bacteria, metabolic modeling, psychrophiles, *Shewanella*, thermodynamics

Temperature has a major impact on microbial physiology, affecting growth through physicochemical changes such as altered enzyme stability (1–3), reaction kinetics (1), and membrane fluidity (4). Mesophilic organisms are known to respond to nonoptimal

**Editor** Rachel Mackelprang, California State University, Northridge

**Copyright** © 2022 Dufault-Thompson et al. This is an open-access article distributed under the terms of the [Creative Commons Attribution 4.0 International license](https://creativecommons.org/licenses/by/4.0/).

Address correspondence to Ying Zhang, yingzhang@uri.edu, or Fengping Wang, fengpingw@sjtu.edu.cn.

\*Present address: Keith Dufault-Thompson, National Library of Medicine, National Institutes of Health, Bethesda, Maryland, USA.

The authors declare no conflict of interest.

**Received** 1 July 2022

**Accepted** 22 July 2022

**Published** 11 August 2022

growth temperatures by using a variety of strategies, such as the induction of cold or heat shock proteins (5–9), alteration of gene expression patterns (10), adjustment of membrane lipid composition (4), modification of protein synthesis and degradation (11, 12), and broad remodeling of metabolic pathways (10, 13, 14). A common cellular response to changes in temperature is the alternation of ATP levels in the cell, though variable responses have been seen among species adapted to different environments (15, 16). Additionally, the ability of bacteria to utilize ATP efficiently during the production of proteins and other biomass components has been shown to vary greatly in different conditions and at different growth rates (17, 18). Changes in temperature can also affect biogeochemical cycling by driving changes in the carbon use efficiency (CUE) of microbial communities (19). However, the influence of temperature on CUE is variable between different microbes and even within the same taxa (20). Overall, these prior studies demonstrate that responses to temperature changes can involve multiple physiological changes and be highly diverse among organisms.

Compared to the extensive understanding of temperature-related physiological responses in mesophiles, a comprehensive view of these processes is still being developed for psychrophiles, organisms having maximum growth temperatures around 20°C, and optimal growth temperatures between 5°C and 15°C. Unlike the mesophiles, some psychrophiles constitutively express proteins commonly involved in cold shock responses (21, 22). A variety of metabolic responses can be induced in psychrophilic or psychrotolerant organisms under low-temperature conditions (23), including the differential expression of genes related to electron transport, carbon utilization, and energy production, along with the upregulation of the biosynthesis of branched-chain amino acids and unsaturated fatty acids (23–27). At elevated temperatures, psychrophiles have been observed to respond through the upregulation of heat shock proteins (28) and changes in the regulation of energy metabolism (15, 29, 30).

The psychrophilic bacterium, *Shewanella psychrophila* WP2 (here referred to as WP2), was isolated from benthic sediments in the western Pacific Ocean, where the ambient environmental temperature was approximately 4°C (31). WP2 has an optimal growth temperature of 10 to 15°C and a growth range of 0 to 20°C, and it exhibits the hallmark metabolic versatility seen in the *Shewanella* genus (31, 32). WP2 belongs to group 1 *Shewanella*, a clade mainly consisting of deep-sea strains characterized by their tolerance and adaptation to low-temperature and high-pressure conditions (33, 34). WP2 represents a distinct clade that is distant from two other group 1 *Shewanella* strains that have been represented using genome-scale models (GEMs), *Shewanella loihica* PV-4 and *Shewanella piezotolerans* WP3 (33, 35). An analysis of the complete genome of WP2 revealed an expansion of transposable elements, motility genes, and chemotaxis genes compared to other deep-sea *Shewanella* (36). However, so far, little is known about the mechanisms of its psychrophilic adaptation or its physiological responses to nonoptimal temperatures.

Genome-scale metabolic modeling has become a common technique for investigating genotype-phenotype associations in bacteria. Advancements in the development of GEMs have enabled their application in mapping metabolic responses of a growing number of extremophilic organisms under diverse environmental conditions (37–39). Constraint-based approaches are commonly used to simulate the utilization of metabolic pathways in GEMs, where optimal solutions of an objective function (e.g., biomass production by a microorganism) are explored within the boundary of predefined metabolic constraints (e.g., the stoichiometric constraints of biochemical reactions) (40, 41). Extensions of typical constraint-based approaches are often centered around the definition of additional constraints and exploration of the solution space. For example, constraints related to the thermostability of metabolic enzymes can be introduced based on the analyses of three-dimensional protein structures, leading to the identification of growth-limiting metabolic steps of a mesophilic bacterium under supraoptimal temperatures (42). Thermodynamics-based metabolic flux analysis (TMFA) uses thermodynamic constraints to inform the feasibility of reactions, permitting the incorporation of additional variables, including

temperature, metabolite concentrations, and Gibbs free energy change of reactions ( $\Delta_r G'$ ), into the model representation (43, 44). While changes in thermodynamic favorability due to temperature are known to have effects on metabolic pathway utilization (45–47), methods like TMFA have not been extensively applied to simulate metabolism at different temperatures.

To build toward a systems-level understanding of the metabolic responses of psychrophilic bacteria to different temperatures, thermodynamic constraints were applied during the modeling of temperature-dependent metabolic changes in WP2, a deep-sea psychrophilic bacterium. The predicted metabolic pathway utilization and metabolic efficiency measures were compared among different growth temperatures to investigate the underlying mechanisms involved in temperature acclimation in WP2.

## RESULTS

**Temperature-dependent, thermodynamically constrained genome-scale models of WP2.** A genome-scale metabolic reconstruction was developed following the iterative annotation of the WP2 genome (GenBank assembly accession no. [GCA\\_002005305](https://www.ncbi.nlm.nih.gov/assembly/GCA_002005305)) (Materials and Methods). The resulting WP2 GEM had an overall consistency score of 99% based on the MEMOTE test suite (48) and contained 940 reactions, 786 genes, and 683 metabolites (see Data Set S1 in the supplemental material). It represents experimentally confirmed growth and no-growth phenotypes on combinations of carbon sources (e.g., glucose, galactose, cellobiose, etc.) and electron acceptors [e.g., nitrate, trimethylamine *N*-oxide, Fe(III), etc.] (Table 1 in Data Set S1). The construction of temperature-dependent, thermodynamically constrained models was performed using the TMFA approach (Materials and Methods). Thermodynamic constraints were included for 89% (839 reactions) of the 940 reactions included in the WP2 GEM, with the rest of the reactions either representing macromolecular biosynthesis or involving complex metabolites that have unknown Gibbs free energies of formation (Data Set S1). Temperature dependency was introduced through the calculation of Gibbs free energy change of reactions ( $\Delta_r G'$ ) for the representation of models under optimal (15°C), supraoptimal (20°C), and suboptimal (4°C) temperatures (Materials and Methods).

Each temperature-dependent model was calibrated by using experimentally measured growth rates to constrain an ATP hydrolysis reaction (ATPM) that accounts for the non-growth-associated ATP utilization by a cell. Briefly, this ATP maintenance flux was determined by fitting the model predictions to experimentally measured growth rates (Fig. 1A), and the constraint range of the ATP maintenance flux was determined based on the experimentally derived growth rates of three biological replicate cultures of WP2 grown at each temperature (Materials and Methods). The lowest ATP maintenance cost was observed under 15°C, with a calibrated ATP hydrolysis constraint ranging between 1.32 and 1.36 (Fig. 1B). Compared to the 15°C condition, the calibrated ATP maintenance constraint was doubled under 4°C, ranging between 2.71 and 2.82 (Fig. 1C). The 20°C model had much higher ATP maintenance cost and also higher variability in the calibrated ATP hydrolysis constraint than the 15°C or 4°C models, ranging between 7.41 and 11.55 (Fig. 1D). This aligned with the lower growth rate and a greater level of growth variability (as measured by the standard deviations of the growth yields under each sampling point) across experimental replicates at 20°C. The ATP maintenance constraints were applied for all subsequent simulations of the corresponding temperature-dependent models unless otherwise noted.

**Temperature-dependent changes in metabolic efficiency.** The temperature-dependent models were simulated with *N*-acetyl-D-glucosamine (GlcNac) as a sole carbon source in aerobic conditions, replicating the conditions used in the WP2 growth experiments (Materials and Methods). For each temperature-dependent model, 1,000 random simulations were performed, with each simulation constrained by fixing the biomass flux to a random value selected within the range of experimentally derived growth rates (Materials and Methods). Predictions of reaction fluxes, Gibbs free energy change of reactions, and metabolite concentrations were generated from each random simulation and were used to characterize the metabolic changes between different temperatures.

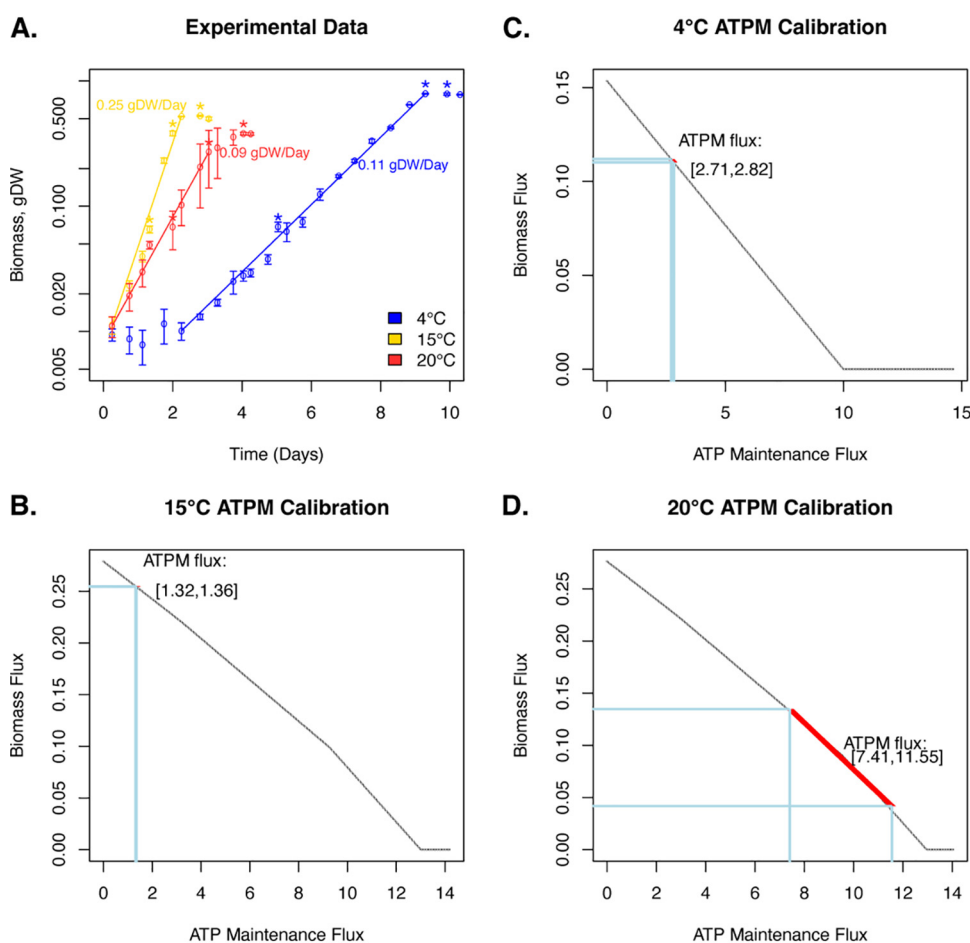


**FIG 1** Temperature-dependent calibration of metabolic constraints on the non-growth-associated ATP maintenance. (A) Experimental measurements of WP2 growth under 4°C (blue), 15°C (yellow), and 20°C (red). The open circles and error bars represent the average and standard deviation of growth yields, measured at each time point over three biological replicates. The solid lines indicate periods of exponential growth at each condition. Labels indicate the average growth rate from each temperature over three biological replicates. Asterisks indicate time points where transcriptome sequencing (RNA-Seq) samples were taken. (B to D) Calibration of the ATPM fluxes in the 15°C (B), 4°C (C), and 20°C (D) models based on experimental data. Successively increasing ATPM fluxes (x axis) were plotted against the optimized biomass fluxes (y axis) determined from the robustness simulation. Horizontal lines were used to indicate the range of experimentally determined growth rates. Vertical lines were used to indicate the range of calibrated ATPM fluxes.

The metabolic efficiency was estimated based on each random simulation using three global efficiency parameters, CUE, ATP production per carbon substrate (ATP-produced/GlcNac), and ATP consumption per gram dry weight (gDW) of biomass (Materials and Methods). Of the three temperature-dependent models, the 15°C model showed the highest metabolic efficiency, with a high CUE (2- to 3-fold higher than what was predicted in 4°C or 20°C models), a high ATP production, and a low ATP consumption in biomass synthesis (Fig. 2). While the 4°C and 20°C models had similar CUE, they showed distinct profiles in both ATP production and ATP consumption. The 20°C model was characterized by a high level of metabolic variability. It had an overall higher ATP production and higher ATP consumption than the other two models. The 4°C model, in contrast, demonstrated the lowest ATP production per carbon substrate. The predicted ATP consumption in biomass synthesis under 4°C was higher than the 15°C model but, on average, lower than the 20°C model (Fig. 2).

**Temperature-dependent remodeling of metabolic pathway usage.** Comparisons of the  $\Delta_r G'$  and reaction fluxes predicted from the 1,000 random simulations revealed a broad, temperature-dependent remodeling of metabolic pathway utilization in WP2. Of the 940 metabolic reactions, significant changes in metabolic flux were identified

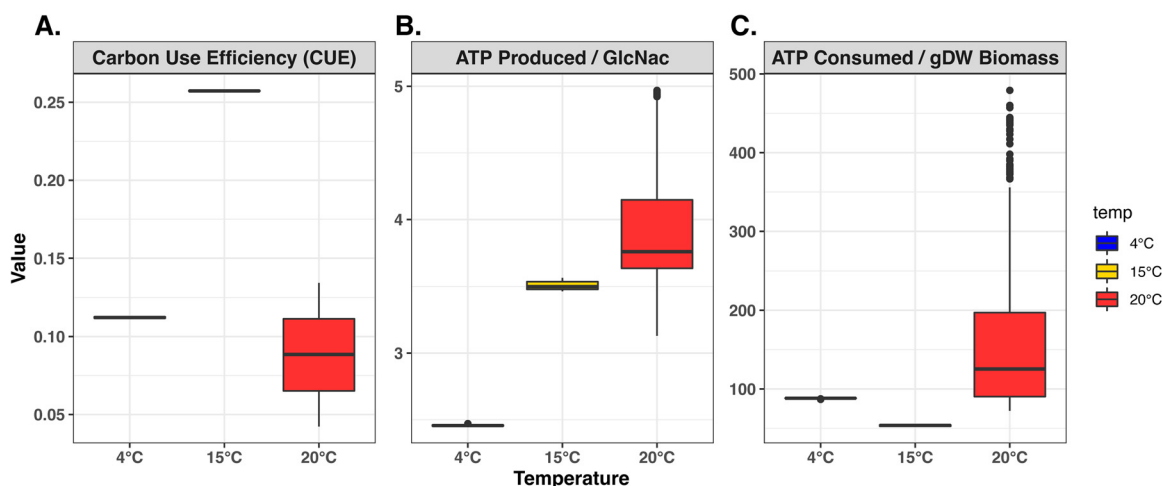


**FIG 2** Predictions of metabolic efficiency by the temperature-dependent models. (A to C) Boxplots showing the carbon use efficiency (A), ATP produced per unit of carbon source (B), and ATP consumed per gram dry weight of biomass (C) predicted by the 4°C (blue), 15°C (yellow), and 20°C (red) models based on 1,000 random simulations.

for 326 (35%) reactions, and significant changes in  $\Delta_r G'$  were observed in 259 (28%) reactions (Data Set S2).

Multiple differences were observed in the utilization of central metabolic pathways under the different temperatures (Fig. 3). One of the main differences was related to how the temperature-dependent models utilize the payoff phase of glycolysis, which catalyzes the chemical conversion from glyceraldehyde 3-phosphate (G3P) to phosphoenolpyruvate (PEP), generating cellular energy in the form of ATP and reduced forms of electron carriers (i.e., NADH). The pathway was predicted to carry flux in both the 15°C and 20°C models; however, it was blocked under 4°C due to the glyceraldehyde-3-phosphate dehydrogenase (GAPD) reaction being thermodynamically unfavorable at the lower temperature. Instead, the carbon flow in the 4°C model was redirected through the gluconeogenic reactions, fructose biphosphate aldolase (FBA), and fructose biphosphatase (FBP) toward the oxidative pentose phosphate pathway (PPP) and the Entner-Doudoroff (ED) pathway. The utilization of the oxidative PPP and ED pathways was optional in the 15°C or 20°C models.

The 4°C model also differed from the 15°C or 20°C models in its utilization of the phosphate acetyltransferase (PTAr) reaction (Fig. 3). PTAr was thermodynamically constrained to carry flux in the acetyl-phosphate (AcP) to acetyl-CoA (AcCoA) direction in the 4°C model, likely contributing to carbon conservation through the production of AcCoA. In contrast, the PTAr reaction in the 15°C and 20°C models carried flux in the AcCoA-consuming direction and was linked to the downstream production of ATP and acetate via the acetate kinase reaction (ACKr).

The three temperature-dependent models also varied in their utilization of the tricarboxylic acid (TCA) cycle. The 4°C model used the isocitrate lyase (ICL), fumarase (FUM), and malic enzyme (ME2) reactions, conserving carbon for the production of pyruvate (PYR), which, in turn, could be used for the synthesis of the precursor metabolites, PEP and AcCoA (Fig. 3). The FUM and ME2 reactions were used in the 15°C model but were optional in the 20°C model, while the ICL reaction was not used under 20°C and was optional under 15°C.

Outside the central carbon metabolism, differences were also observed in the modeled utilization of the electron transport system. The ATP synthase reaction (ATPS4r) was used in the proton-pumping direction in the 15°C model and was optional in the same direction in the 20°C model. However, ATPS4r was not used in the 4°C model. The 20°C model obligately used the proton-translocating NADH/quinone oxidoreductase reactions (NADH11, NADH13, and NADH16) to carry out electron transport from NADH to the quinone pool. This was connected to the fumarate reductase reaction (FRD10 and FRD11), apparently contributing to the cycling of electron carriers in the 20°C model. In contrast, the 4°C model

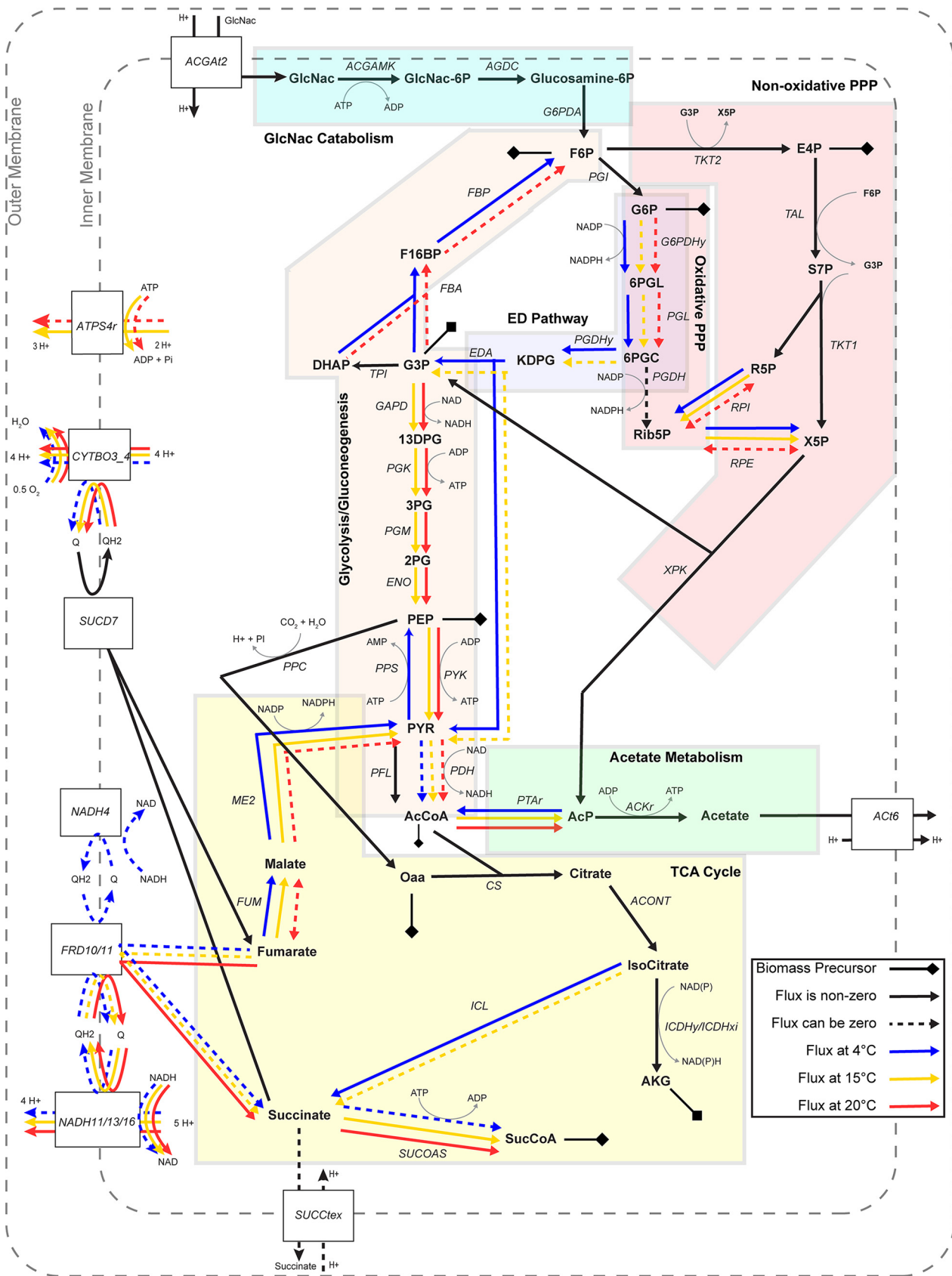


**FIG 3** Temperature-dependent utilization of metabolic pathways. Pathway diagram showing the direction of metabolic fluxes predicted by the different models. Solid lines indicate reactions that are obligated to carry nonzero fluxes in the shown direction, while dashed lines indicate that (Continued on next page)

could utilize the alternative, non-proton-translocating NADH dehydrogenase reaction (NADH4), which was not used in either the 15°C or the 20°C model (Fig. 3). Overall, higher variability and lower fluxes were seen in the electron transport reactions (e.g., SUCD7, CYTBO3\_4, FRD10, FRD11, NADH11, NADH13, and NADH16) in the 4°C model than the 15°C or 20°C models (Fig. S1).

The remodeling of electron transport pathways was reflected in the changes of the overall redox potential, measured by the ratios between concentrations of reduced versus oxidized forms of electron carrier metabolites (Fig. 4). The 4°C model demonstrated the highest [NADH]/[NAD<sup>+</sup>] and [NADPH]/[NADP<sup>+</sup>] ratios, which may indicate the conservation of reducing equivalents and was consistent with the reduced metabolic fluxes in the electron transport system, such as the NADH/quinone oxidoreductase (Fig. S1). Surprisingly, despite a predicted low ATP production efficiency and a high ATP consumption for biomass synthesis in the 4°C model (Fig. 2), a higher [ATP]/[ADP] ratio was observed in the 4°C model than the 15°C or the 20°C models (Fig. 4), suggesting a high level of energy conservation at the low temperature.

**Differential expression of metabolic genes.** The temperature-dependent metabolic responses of WP2 were experimentally characterized using transcriptomes obtained from three growth phases, early exponential, late exponential, and stationary (Materials and Methods). Comparisons of the transcriptomes revealed a very weak negative correlation between the expression of genes at 4°C compared to the other two temperatures, similar to what was observed on the model-predicted metabolic fluxes and  $\Delta_rG'$  values (Fig. S2). Analyses of the expression of genes associated with specific metabolic reactions showed a great level of variability across different growth phases (Data Set S3) but also revealed agreement between the differential expression of genes and the temperature-dependent differences in fluxes of some key reactions from the carbon metabolism and electron transport pathways, especially during the late exponential growth phase (Fig. S1).

The pyruvate formate lyase (PFL) gene was significantly upregulated under 15°C in the late exponential phase. This was consistent with the high metabolic flux predicted for the PFL reaction and the prediction of a more active glycolytic pathway, an upstream pathway to PFL, in the 15°C model. The expression of the PFL gene at 20°C was higher than 4°C during the early exponential phase but lower than 4°C during the late exponential or stationary phases. This was in line with the high variability of PFL metabolic fluxes in the 20°C model.

Other examples of differentially expressed genes were observed in the central carbon metabolism. Genes encoding the FBA, glucose-6-phosphate dehydrogenase (G6PDH), and phosphogluconate dehydratase (PGDH) reactions were upregulated under 4°C (Fig. S1). This was consistent with the model-predicted utilization of the oxidative PPP and ED pathways under 4°C (Fig. 3). The ICL gene was similarly upregulated under 4°C in the late exponential phase. This was also in line with the model-predicted use of ICL in the 4°C model. The PTAr gene was upregulated under 15°C and 20°C compared to 4°C, corresponding with the predicted higher magnitude of PTAr fluxes under these optimal and supraoptimal temperatures (Fig. S1).

Additional examples involved the differential expression of genes in the electron transport systems. Specifically, multiple genes encoding subunits of the ATP synthase and the proton-translocating NADH/quinone oxidoreductase were upregulated under

### FIG 3 Legend (Continued)

the reaction flux was zero in some instances of the 1,000 random simulations. Black lines represent common pathways used by WP2 under all three temperatures. Colored lines represent pathways used under 4°C (blue), 15°C (yellow), or 20°C (red). Metabolic pathways were shown with background shades and labeled by the pathway name. Precursor metabolites for biomass production are marked with a line capped with a diamond. Abbreviations: GlcNac: *N*-acetyl-D-glucosamine; GlcNac-6P, *N*-acetyl-D-glucosamine 6-phosphate; glucosamine-6P, D-glucosamine 6-phosphate; F6P, D-fructose 6-phosphate; F16BP, D-fructose 1,6-bisphosphate; DHAP, dihydroxyacetone phosphate; G3P, glyceraldehyde 3-phosphate; 13DPG, 3-phospho-D-glyceroyl phosphate; 3PG, 3-phospho-D-glycerate; 2PG, D-glycerate 2-phosphate; PEP, phosphoenolpyruvate; PYR, pyruvate; AcCoA, acetyl-CoA; G6P, D-glucose 6-phosphate; 6PGL, 6-phospho-D-glucono-1,5-lactone; 6PGC, 6-phospho-D-gluconate; Rib5P, D-ribose 5-phosphate; KDPG, 2-dehydro-3-deoxy-D-gluconate; E4P, D-erythrose 4-phosphate; S7P, sedoheptulose 7-phosphate; R5P, alpha-D-ribose 5-phosphate; X5P, D-xylulose 5-phosphate; AcP, acetyl phosphate; Oaa, oxaloacetate; AKG, 2-oxoglutarate; SucCoA, succinyl-CoA; malate, L-malate; Pi, orthophosphate; H<sup>+</sup>, proton; QH2, quinol pool; Q, quinone pool.

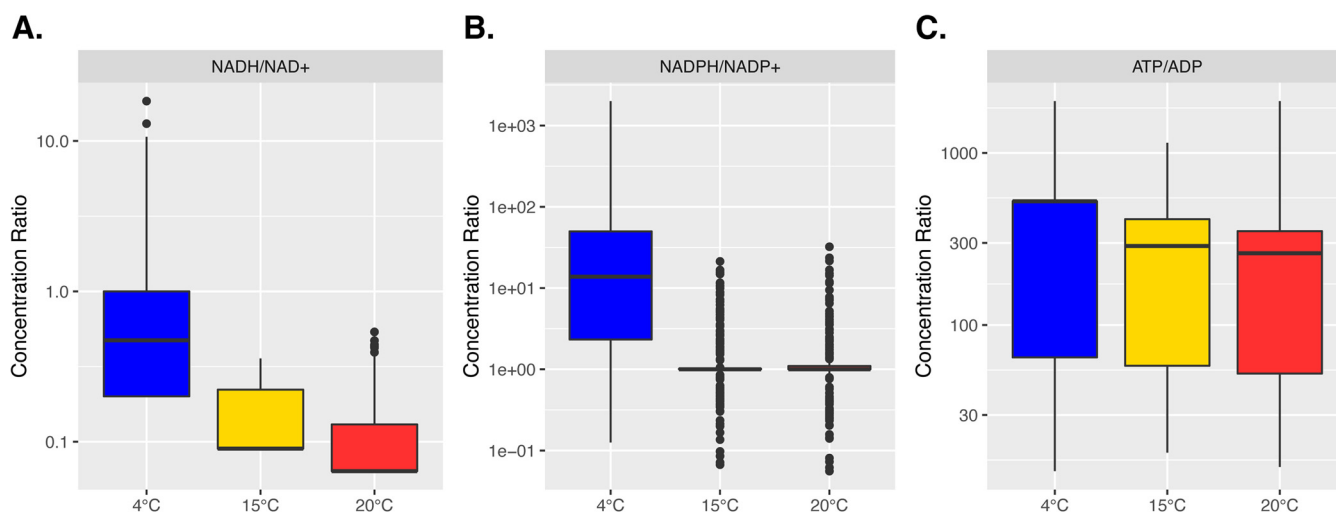


**FIG 4** Ratios of metabolite concentrations predicted by the temperature-dependent models. (A to C) Ratios of  $[NADH]/[NAD^+]$  (A),  $[NADPH]/[NADP^+]$  (B), and  $[ATP]/[ADP]$  (C) are shown as boxplots based on 1,000 random simulations for the 4°C (blue), 15°C (yellow), and 20°C (red) models.

20°C compared to 4°C, and the non-proton-translocating NADH dehydrogenase was upregulated at 4°C compared to 20°C. These were consistent with the model predictions, as the 20°C model predicted higher fluxes through the NADH11, NADH13, and NADH16 reactions, and the 4°C model predicted the potential usage of NADH4 and lack of utilization of ATP54r (Fig. S1).

## DISCUSSION

Genome-scale metabolic modeling has been applied to a variety of different biological problems, but the incorporation of complex environmental factors like pH, pressure, or temperature into simulations of growth remains challenging. In this study, thermodynamically constrained models were developed of WP2, a deep-sea psychrophilic bacterium, setting an example for modeling metabolic responses to different temperatures.

The temperature-dependent, thermodynamically constrained models were calibrated based on experimentally measured growth of WP2 under optimal (15°C), suboptimal (4°C), and supraoptimal (20°C) temperatures, suggesting the lowest ATP maintenance cost in the 15°C model and a 2- and 7-fold-higher ATP maintenance cost in the 4°C and 20°C models, respectively (Fig. 1). Higher variability was predicted in the calibrated range of ATP maintenance fluxes in the 20°C model than the 15°C or 4°C models, which can be attributed to the greater variability among replicates of the growth experiments. Interestingly, the experimental replicates from 20°C revealed an earlier start of the exponential growth phase but a lower average growth rate than the suboptimal temperature of 4°C (Fig. 1). This may indicate potential growth deficiency under 20°C, likely due to high-temperature stress, as 20°C represents the highest temperature that WP2 is known to grow at (32).

To provide a quantitative estimation of the metabolic efficiency, three global parameters, including the CUE, the ATP production per carbon substrate, and the ATP consumption per gDW of biomass synthesis, were calculated for each temperature-dependent model based on metabolic fluxes from 1,000 rounds of random simulations (Materials and Methods). These global parameters revealed the highest metabolic efficiency in the 15°C model, characterized by high CUE, high ATP production per carbon substrate, and low ATP consumption compared to the other two temperatures. The predicted CUE under 15°C had a median value of 0.26 (Fig. 2). This was similar to values predicted for other bacteria in substrate-limited growth conditions (49), indicating similar levels of metabolic efficiency in WP2 during optimal growth.

The two models of nonoptimal temperatures (4°C and 20°C) predicted similar CUE but distinct measures of ATP production and ATP consumption (Fig. 2). The 4°C model

had low efficiency in ATP production and moderately high ATP consumption in biomass synthesis, while the 20°C model had high ATP production and even higher ATP consumption in biomass synthesis than the 4°C model. It is worth mentioning that our calculation of the ATP consumption did not include the non-growth-associated ATP maintenance (ATPM) for each temperature-dependent model. Therefore, the predicted high ATP consumption in 4°C and 20°C models should reflect the high metabolic demands for each unit of biomass synthesis under these nonoptimal temperatures.

The suboptimal temperature modeled in this study (4°C) represents the ambient temperature of WP2 in the deep sea (32). Our modeling result may indicate that WP2 is characterized by slow growth, with low CUE and low ATP production in its natural environment. This is similar to the slow-growth phenotypes that have been observed in other deep-sea microbes (50, 51). Interestingly, slow growth has also been proposed as a survival strategy in bacteria, allowing them to better survive in oligotrophic or other extreme conditions (52–54). The 20°C model, while representing the highest tolerable temperature for WP2, presented the lowest growth rate and highest variability in the model-predicted metabolic fluxes. It has been suggested that this kind of flux variability may be related to a growth-flexibility trade-off, where slower growth may facilitate the use of alternative metabolic pathways while adjusting to environmental changes (55).

The temperature-dependent changes in metabolic efficiency may be linked to altered metabolic pathway usage predicted under the different temperatures. The higher ATP production in 15°C and 20°C models could be attributed to the utilization of the payoff phase of glycolysis (Fig. 3), as the ATP-generating reactions in this pathway (e.g., PGK and PYK) were utilized in 15°C and 20°C models but blocked under 4°C due to unfavorable thermodynamics of the GAPD reaction (see Data Set S2 in the supplemental material). The downstream reaction, PFL, accordingly carried higher fluxes in the 15°C and 20°C models than the 4°C model, consistent with the experimentally observed upregulation of the PFL gene under the higher temperatures (Fig. S1). The decrease of glycolytic fluxes in WP2 under 4°C was similar to the low-temperature responses observed in other psychrophilic bacteria (25, 26, 56), suggesting that the differential use of glycolysis may be driven by the thermodynamics of this pathway in low-temperature conditions.

The absence of glycolysis flux under 4°C led to the redirection of metabolic fluxes through the oxidative PPP and ED pathways. This was again consistent with the upregulation of genes associated with these pathways (e.g., FBA, G6PDH<sub>y</sub>, and PGDH<sub>y</sub>) (Fig. S1). It has been documented that the glycolytic pathways have tighter thermodynamic bottlenecks than the ED pathway (57), and the ED pathway is known to have a lower protein synthesis cost (17, 58). A similar metabolic strategy has also been reported in another psychrophilic gammaproteobacterium, *Colwellia psychrelythraea* (59).

Additional temperature-dependent alternations of metabolic pathway usage were observed in the TCA cycle and the electron transport chain (Fig. 3). The use of the ICL reaction in the 4°C model was consistent with the upregulation of the ICL gene under 4°C in the late exponential phase (Fig. S1). Similarly, the upregulation of non-proton-translocating NADH dehydrogenase under 4°C aligned with the utilization of NADH<sub>4</sub> reaction in the 4°C model (Fig. S1). The ICL reaction is considered to be a route for carbon conservation, as it bypasses the CO<sub>2</sub>-producing steps in the TCA cycle (60). The upregulation of ICL has been observed under other stress conditions, such as oligotrophy or Fe limitation, and has been linked to the reduction of electron transport activity (61, 62). This potentially aligns with the prediction of relatively lower metabolic fluxes carried by the NADH/quinone oxidoreductase (NADH<sub>11</sub>, NADH<sub>13</sub>, and NADH<sub>16</sub>) in the 4°C model and is consistent with the gene expression data, especially in contrast to the 20°C condition (Fig. S1). Considering that our models predicted higher [NADH]/[NAD<sup>+</sup>] and [NADPH]/[NADP<sup>+</sup>] ratios under 4°C (Fig. 4), metabolic remodeling in the TCA cycle and electron transport systems may reflect potential shifts in the intracellular redox balance under the suboptimal temperature.

The ATPS<sub>4r</sub> was predicted to carry flux in the 15°C or the 20°C models, but not in the 4°C model (Fig. 3). Consistent with these temperature-dependent predictions, significant upregulation of genes encoding multiple subunits of the ATP synthase was observed in

the late exponential phase when comparing transcriptomes in 15°C or 20°C to 4°C (Data Set S3). The ATP54r reaction, when carrying non-zero fluxes, was predicted to run only in the ATP-consuming, proton-pumping direction (Fig. 3), similar to what has been observed in other *Shewanella* species (33, 63). The lack of ATP54r flux in the 4°C model likely reflects a mechanism of ATP conservation. This was consistent with the higher [ATP]/[ADP] ratio predicted in the 4°C model than in the 15°C or 20°C models (Fig. 4). It has been documented that psychrophilic organisms increase intracellular ATP levels in response to lower temperatures despite their reduced growth rates (15, 64). Our modeling results were consistent with these observations and suggested that WP2 may carry out similar responses to other psychrophiles under low temperatures.

Overall, our reconstruction of thermodynamically constrained genome-scale models provided an integrated view of the metabolic responses to different temperature conditions by a deep-sea psychrophilic bacterium. Several temperature-dependent changes in metabolic efficiency, pathway usage, and metabolite ratios were predicted by the models, demonstrating the complexity of metabolic responses under optimal and nonoptimal temperatures. Future developments of this approach may include the incorporation of physiological changes associated with growth in different temperatures, such as altered membrane structures and changes in biomass composition. The modeling approach can be broadly applied to study temperature-dependent adaptations of other organisms, contributing to a systems-level understanding of metabolic responses to changing temperatures.

## MATERIALS AND METHODS

**WP2 growth experiments.** Inoculations of three biological replicates for each growth temperature (4°C, 15°C, and 20°C) were performed in 150 mL of fresh LMO-812 media (33) with 1 mL of inoculum obtained from cultures grown to exponential phase at the optimal temperature (15°C) in marine medium 2216 (Difco). The cultures were grown with 5 mM GlcNac as the sole carbon source in aerobic conditions at each temperature with shaking, and an initial optical density at 600 nm ( $OD_{600}$ ) of 0.002 was measured for each inoculation. Turbidity was monitored throughout the growth phases of the cultures, and the  $OD_{600}$  values were converted to gram dry weight values for each culture using a previously established relationship between OD and dry weight biomass in *Shewanella* (65). Growth rates were calculated based on the periods of exponential growth for each temperature condition (Fig. 1).

**Transcriptome sampling and differential gene expression analysis.** Samples for transcriptome sequencing were taken from the early exponential, late exponential, and stationary phases for each replicate in the 4°C, 15°C, and 20°C cultures (Fig. 1). Two biological replicates were sampled from each of the targeted growth phases for each temperature, where 2 mL of culture was taken from each replicate and centrifuged at  $12,000 \times g$  for 2 min, and the cell pellet was used for the application of RNA extraction and sequencing services provided by the Sangon Biotech in Shanghai, China. Total RNA was extracted from the cell pellets and cleaned using the Ribo-off rRNA depletion kit. cDNA libraries were prepared using the VAHTS stranded mRNA-seq V2 library prep kit for Illumina. Paired-end sequencing was performed on the HiSeq X Ten system generating  $2 \times 150$ -bp reads.

Raw transcriptome reads were quality filtered using Trimmomatic version 0.33 (66) based on the following criteria: (i) remove any leading or lagging bases with quality scores less than 20, (ii) clip off any Illumina adapters, (iii) scan the read with a 5-base-wide sliding window and cut when the average quality score per base drops below 20, and (iv) remove any sequences shorter than 50 bp. The trimmed reads, both paired and unpaired, were then mapped to the WP2 genome using BMAP version 38.81 (66), with all default settings except for requiring a minimum identity for mapping of 90%. The mapped reads were then used to generate count tables of the number of transcripts that map to each gene using the featureCounts program version 1.6.3 (67) with default settings. Differential expression of genes was identified between different temperatures in each growth phase using DESeq2 version 1.22.2 (68). Genes were considered to be significantly differentially expressed if the  $\log_2$  fold change between conditions was greater than 1 or less than  $-1$  and if the adjusted  $P$  value was less than or equal to 0.05. The gene expression data (see Fig. S1 in the supplemental material) were visualized using the `geom_boxplot` function in the R package ggplot2 (version 3.3.5) to present the median ratio normalization (MRN) values from replicate samples at each growth phase. If multiple genes were associated with a reaction, the expression levels of each gene were included as a data point in the box plot.

**Genome-scale metabolic reconstruction.** A genome-scale model was constructed for WP2 based on ortholog mapping and manual curation. Protein sequences were downloaded from the GenBank assembly database for the full genomes of *S. psychrophila* WP2 (GCA\_002005305), *S. piezotolerans* WP3 (GCA\_000014885), *S. oneidensis* MR-1 (GCA\_000146165), *Shewanella* sp. strain MR4 (GCA\_000014685), *Shewanella* sp. strain W3-18-1 (GCA\_000015185), and *S. denitrificans* OS217 (GCA\_000013765). Orthologous genes between the genomes were identified using a bidirectional best hit BLASTp approach as detailed in a previous study (69). The `psamotate` function in the PSAMM software package version 1.1 (70) was used to generate a draft model of WP2 based on the predicted orthologous genes and previously published GEMs of *S. piezotolerans* WP3 (33), *S. oneidensis* MR-1 (65), *Shewanella* sp. MR4,

*Shewanella* sp. W3-18-1, and *S. denitrificans* OS217 (71) (Table 2 in Data Set S1). Following the initial reconstruction, eggNOG-mapper (version 1) (72, 73) was used to assign putative functions to the WP2 genes based on the eggNOG database version 5.0 (74) and to map WP2 genes to the Kyoto Encyclopedia of Genes and Genomes (KEGG) (75) and COG (76) databases. These functional assignments were manually curated to identify functions and genes missing from the draft model. A biomass objective function for WP2 was constructed based on the genome sequence, predicted coding sequences, and predicted proteome of WP2 (36) (Table 3 in Data Set S1). The fatty acid composition of the WP2 model was calculated based on the experimentally measured lipid composition in WP2 (32), and the trace element component of the biomass was formulated based on the values used in the iJO1366 *Escherichia coli* GEM (77). This biomass formulation was used for simulations performed at all three temperatures.

Metabolic gaps in the WP2 model were identified using the fastgapfill (78) and gapfill (79) functions as implemented in PSAMM version 1.1. The gap-filling process was performed using LMO-812 medium (33) with experimentally verified combinations of carbon sources and electron acceptors (32). Reactions from template models of other *Shewanella* species, the iJO1366 *E. coli* model (77), and the BIGG database version 1.5 (80) were used as references for the gap filling. Metabolic reactions predicted by the gap-filling step were included in the model when a corresponding gene was identified in the WP2 genome. Gap reactions were added to the model without gene associations only if they were required for the model to produce biomass (Table 4 in Data Set S1). Charge and mass balance in the WP2 model was verified using the chargecheck, formulacheck, and masscheck functions in PSAMM version 1.1 (70). Model stoichiometric consistency, mass balance, charge balance, and metabolite connectivity were further verified using MEMOTE software (48). The complete WP2 GEM was compared to previously reported growth phenotypes for WP2 to confirm that it can utilize the experimentally verified carbon sources and electron acceptors for growth (Table 1 in Data Set S1).

**Identification of thermodynamic constraints.** Standard Gibbs free energy change of reaction ( $\Delta_r G'^{\circ}$ ) was calculated for reactions in the WP2 model using the group-contribution python package (81) (Table 5 in Data Set S1). Multiple settings for the group-contribution prediction were tested to evaluate the effects of the pH and ionic strength parameters on the predicted  $\Delta_r G'^{\circ}$  values. Only small differences were observed in the predictions when different settings were used, and due to these properties being unknown in WP2, the standard condition for the  $\Delta_r G'^{\circ}$  estimation was defined as pH 7, ionic strength of 0 M, and 25°C. In order to run the group-contribution approach on individual reactions in the WP2 model, all metabolites participating in a reaction were represented in one of two forms, (i) identifiers in the Thermodynamics of Enzyme-Catalyzed Reactions Database (TECRDB) (82), which provides thermodynamic data for a collection of enzyme-catalyzed reactions; or (ii) metabolite structure represented as Simplified Molecular-Input Line-Entry System (SMILES) strings (Table 6 in Data Set S1), which can be used to derive information related to metabolite properties for the  $\Delta_r G'^{\circ}$  calculation. Metabolites in the WP2 model were first mapped to the TECRDB based on their names and formulas, and when a mapping was not available, metabolite structural information was collected from the PubChem database (83) in the form of the canonical SMILES strings. When SMILES strings were not available in the PubChem database, for example, for chitin, eicosapentaenoic acid (EPA), 3-hydroxy-11-methyldodecanoic acid, 11-octadecenoic acid, and the fatty-acyl ACP compounds, metabolite structures were manually drawn using the MarvinSketch application version 19.11 (ChemAxon; <https://www.chemaxon.com>) and exported using the SMILES export function. Artificial metabolites representing macromolecule biomass components like DNA, RNA, and the overall biomass compound were not assigned SMILES strings. The  $\Delta_r G'^{\circ}$  of the biomass objective function, macromolecular biosynthesis reactions, and several reactions in the cell wall biosynthesis pathway were not predicted due to the complexity of the metabolites involved in these reactions.

**Configuration of the temperature-dependent models.** The TMFA approach (43, 44) was applied to the WP2 model using the tmfa function implemented in PSAMM (version 1.1) in Python version 3.7.10. All simulations were done with the global maximum allowable flux being set to 100 and the minimum allowable flux being set to  $-100$ . The PSAMM tmfa implementation takes as input a configuration file that references the  $\Delta_r G'^{\circ}$  estimations as described in a prior section (Table 5 in Data Set S1), a list of reactions excluded from the  $\Delta_r G'^{\circ}$  calculation due to the high complexity of the involved metabolite's structures (Table 7 in Data Set S1), a list of transport reactions mapped to parameters (i.e., net charge and net protons transported from outside to inside the cell) that can be used to calculate energy associated with electrochemical potential, pH gradient across the cell membrane (Table 8 in Data Set S1), and definitions of metabolite concentrations and exchange constraints (Tables 9 and 10 in Data Set S1). The temperature-dependent simulation of the WP2 model was achieved by introducing a number of constraints that are specific to the growth profiles of the organism under suboptimal, optimal, and supraoptimal temperatures. These included the calculation of  $\Delta_r G'$  values in the TMFA simulation using the temperature in Kelvin, identification of temperature-dependent ATP maintenance constraints, and constraint of oxygen concentrations and exchange fluxes based on the solubility of oxygen at each given temperature.

By default, the concentrations of all metabolites were constrained to be within a range of 1e-5 to 0.02 mol/L following prior studies (43, 84), with the exception of metabolites present in the experimental media and a pair of metabolites involved in an essential metabolic reaction (Table 9 in Data Set S1). First, the concentrations of two metabolites, *N*-carbamoyl-L-aspartate and (*S*)-dihydroorotate, were expanded with a range from 1e-6 to 0.05 mol/L following prior conventions (37) to enable thermodynamic feasibility in an essential dihydroorotase (DHORTS) reaction. Second, the upper bound of oxygen concentration was set according to the solubility of oxygen in liquid media under different temperatures. Next, the compounds that represent nutrient inputs in the LMO-812 media had the upper bound

of their concentrations assigned based on the composition of the media. Finally, the lower bound of media components that had a concentration lower than 1e-4 mol/L was set to 2 orders of magnitude lower than its upper bound to allow for some variability in the concentrations. The pH in the model was constrained between 6 and 8 for both the cytosolic and extracellular compartments.

The exchange flux constraints for the TMFA simulation were formulated to represent the availability of nutrients and the diffusion of metabolic products (Table 10 in Data Set S1). The exchange constraints of carbon, nitrogen, sulfur, and phosphorus sources were constrained based on experimental media. Small molecules and metal ions were released to enable free exchange, and the lower bound of oxygen exchange was set according to the solubility of oxygen in liquid media under different temperatures.

An ATPM reaction was added to each model to account for the non-growth-associated ATP maintenance (Fig. 1). The ATPM reaction was individually calibrated for each temperature-dependent model based on the experimentally measured growth rates. First, a robustness analysis was performed by successively increasing the flux of ATPM while determining the optimized biomass over each step. Next, a linear fitting was performed using the ATPM flux and the biomass flux values. Last, the upper and lower bounds of the ATPM reaction were determined by projecting the experimentally measured growth rates based on the linear fitting (Fig. 1B to D). A range was determined for the ATPM constraint for each temperature-dependent model based on the range of growth rates observed in the experimental replicates of each temperature.

#### Random simulations with temperature-dependent, thermodynamically constrained models.

Metabolic simulations were performed on each temperature-dependent model with the same growth media as in the WP2 growth experiments, using 5 mM GlcNac as the sole carbon source. To probe for the utilization of metabolic pathways under different temperatures, metabolic reaction fluxes,  $\Delta_r G'$ , and metabolite concentrations were predicted by running each model through 1,000 random simulations. Each simulation was performed by constraining the biomass flux to a random value selected within the range of experimentally determined growth rates (0.110 and 0.112 for 4°C, 0.254 and 0.255 for 15°C, and 0.042 and 0.135 for 20°C). The resulting predictions of reaction fluxes,  $\Delta_r G'$ , and metabolite concentrations were summarized by calculating the minimum, maximum, median, and 25th and 75th percentiles over the 1,000 random simulations for each temperature-dependent model (Data Set S2). Significant changes among the temperature-dependent models were identified across the 1,000 random simulations for each metric based on the Kruskal-Wallis test and corresponding pairwise *post hoc* tests, using the `kruskal.test` and the `pairwise.wilcox.test` functions, respectively, in the R package `stats` (version 4.1.3). The effect size was calculated using the `epsilonSquared` function in the R package `rcompanion` (version 2.4.15). Comparisons of the 4°C, 15°C, and 20°C models with effect size  $\geq 0.36$ , following previously established thresholds (85), and with *P* values of  $\leq 0.05$  in both Kruskal-Wallis test and pairwise tests were reported as carrying significant changes across the different temperatures (Data Set S2).

The CUE was calculated from each random simulation using the equation

$$\text{CUE} = \frac{(\text{carbon atoms consumed} - \text{carbon atoms secreted})}{\text{carbon atoms consumed}}$$

following an existing approach (49), where all the carbon-containing exchange compounds were grouped into lists of consumed or produced metabolites based on the direction of their exchange fluxes in a simulation. The exchange fluxes were scaled based on the number of carbon atoms in each compound, and sums of the scaled fluxes were taken for the list of consumed and produced metabolites, respectively, to obtain the carbon atoms consumed and the carbon atom-secreted parameters in the CUE equation.

To calculate the total amount of ATP produced or consumed in a model simulation, the metabolic flux of each reaction that involved ATP was multiplied by the stoichiometry of ATP in that reaction. The resulting positive values indicated the production of ATP, while negative values indicated the consumption of ATP. The flux of the ATPM reaction was excluded from these calculations so that the ATP production and consumption values reported in this study reflected the energy requirements related specifically to the metabolic processes. The ATP production per unit of carbon source was calculated through dividing the sum of all stoichiometrically scaled ATP-producing fluxes by the exchange flux of the carbon source (i.e., GlcNac). The ATP consumed per gDW biomass was calculated through dividing the sum of all stoichiometrically scaled ATP-consuming fluxes by the biomass flux.

The metabolite ratios (Fig. 4) were calculated based on the metabolite concentrations predicted in each random simulation. The visualization of metabolite ratios (Fig. 4), metabolic efficiency metrics (Fig. 2), and individual metabolic fluxes (Fig. S1) was created with the `geom_boxplot` function in the R package `ggplot2` (version 3.3.5), using collections of values obtained from the 1,000 random simulations. Pairwise comparison of  $\Delta_r G'$ , metabolic flux, and gene expression values across different temperature conditions (Fig. S2) were visualized with scatterplots using the `geom_point` function in `ggplot2` (version 3.3.5), with linear fittings visualized with the `stat_smooth` function using the method `lm`. The  $\Delta_r G'$  and metabolic flux were scaled for each reaction across three temperature conditions. This was done by dividing each metric by the root mean square of the same metric across three temperature conditions. The expression values were normalized by MRN and scaled for each individual gene by the root mean square values across three temperatures.

**Data and software availability.** Modeling approaches implemented in this study are accessible through the open-source PSAMM software, release v1.1 and are freely available in a git repository <https://github.com/zhanglab/psamm>. The WP2 GEM in both YAML and SBML formats, all inputs used for the modeling, and all analysis scripts are available on GitHub at the following address: <https://github.com/zhanglab/>

GEM-iWP2. Transcriptome raw read data were deposited in the NCBI Sequence Read Archive database under BioProject accession no. [PRJNA739408](https://www.ncbi.nlm.nih.gov/bioproject/PRJNA739408).

## SUPPLEMENTAL MATERIAL

Supplemental material is available online only.

**FIG S1**, TIF file, 28.2 MB.

**FIG S2**, TIF file, 21.5 MB.

**DATA SET S1**, XLSX file, 1.3 MB.

**DATA SET S2**, XLSX file, 0.4 MB.

**DATA SET S3**, XLSX file, 1.7 MB.

## ACKNOWLEDGMENT

We declare that no competing interests exist.

This project was supported by the National Science Foundation under grant no. 1553211. K.D.-T. was supported in part under the EPSCoR cooperative agreement number OIA-1655221. The experimental work was supported by the National Key R&D Program of China (grant number 2018YFC0310803). Any opinions, findings, conclusions, or recommendations expressed in this material are those of the author(s) and do not necessarily reflect the views of the funders.

## REFERENCES

- DeLong JP, Gibert JP, Lühring TM, Bachman G, Reed B, Neyer A, Montooth KL. 2017. The combined effects of reactant kinetics and enzyme stability explain the temperature dependence of metabolic rates. *Ecol Evol* 7: 3940–3950. <https://doi.org/10.1002/ece3.2955>.
- Romero-Romero ML, Inglés-Prieto A, Ibarra-Molero B, Sanchez-Ruiz JM. 2011. Highly anomalous energetics of protein cold denaturation linked to folding-unfolding kinetics. *PLoS One* 6:e23050. <https://doi.org/10.1371/journal.pone.0023050>.
- Lepock JR, Frey HE, Inniss WE. 1990. Thermal analysis of bacteria by differential scanning calorimetry: relationship of protein denaturation in situ to maximum growth temperature. *Biochim Biophys Acta* 1055:19–26. [https://doi.org/10.1016/0167-4889\(90\)90086-5](https://doi.org/10.1016/0167-4889(90)90086-5).
- Eriksson S, Hurme R, Rhen M. 2002. Low-temperature sensors in bacteria. *Philos Trans R Soc Lond B Biol Sci* 357:887–893. <https://doi.org/10.1098/rstb.2002.1077>.
- Al-Fageeh MB, Smales CM. 2006. Control and regulation of the cellular responses to cold shock: the responses in yeast and mammalian systems. *Biochem J* 397:247–259. <https://doi.org/10.1042/BJ20060166>.
- Phadtare S, Alsina J, Inouye M. 1999. Cold-shock response and cold-shock proteins. *Curr Opin Microbiol* 2:175–180. [https://doi.org/10.1016/S1369-5274\(99\)80031-9](https://doi.org/10.1016/S1369-5274(99)80031-9).
- Yura T, Nagai H, Mori H. 1993. Regulation of the heat-shock response in bacteria. *Annu Rev Microbiol* 47:321–350. <https://doi.org/10.1146/annurev.mi.47.100193.001541>.
- Ermolenko DN, Makhatadze GI. 2002. Bacterial cold-shock proteins. *Cell Mol Life Sci* 59:1902–1913. <https://doi.org/10.1007/pl00012513>.
- Yura T. 2019. Regulation of the heat shock response in *Escherichia coli*: history and perspectives. *Genes Genet Syst* 94:103–108. <https://doi.org/10.1266/ggs.19-00005>.
- Gao H, Yang ZK, Wu L, Thompson DK, Zhou J. 2006. Global transcriptome analysis of the cold shock response of *Shewanella oneidensis* MR-1 and mutational analysis of its classical cold shock proteins. *J Bacteriol* 188: 4560–4569. <https://doi.org/10.1128/JB.01908-05>.
- Perrot F, Hébraud M, Junter G-A, Jouenne T. 2000. Protein synthesis in *Escherichia coli* at 4°C. *Appl Theor Electrophor* 21:1625–1629. [https://doi.org/10.1002/\(SICI\)1522-2683\(20000501\)21:8<1625::AID-ELPS1625>3.0.CO;2-4](https://doi.org/10.1002/(SICI)1522-2683(20000501)21:8<1625::AID-ELPS1625>3.0.CO;2-4).
- Farewell A, Neidhardt FC. 1998. Effect of temperature on in vivo protein synthetic capacity in *Escherichia coli*. *J Bacteriol* 180:4704–4710. <https://doi.org/10.1128/JB.180.17.4704-4710.1998>.
- Hasan CMM, Shimizu K. 2008. Effect of temperature up-shift on fermentation and metabolic characteristics in view of gene expressions in *Escherichia coli*. *Microb Cell Fact* 7:35. <https://doi.org/10.1186/1475-2859-7-35>.
- Beckering CL, Steil L, Weber MHW, Völker U, Marahiel MA. 2002. Genome wide transcriptional analysis of the cold shock response in *Bacillus subtilis*. *J Bacteriol* 184:6395–6402. <https://doi.org/10.1128/JB.184.22.6395-6402.2002>.
- Amato P, Christner BC. 2009. Energy metabolism response to low-temperature and frozen conditions in *Psychrobacter cryohalolentis*. *Appl Environ Microbiol* 75:711–718. <https://doi.org/10.1128/AEM.02193-08>.
- Soini J, Falschlehner C, Mayer C, Böhm D, Weinel S, Panula J, Vasala A, Neubauer P. 2005. Transient increase of ATP as a response to temperature up-shift in *Escherichia coli*. *Microb Cell Fact* 4:9. <https://doi.org/10.1186/1475-2859-4-9>.
- Flamholz A, Noor E, Bar-Even A, Liebermeister W, Milo R. 2013. Glycolytic strategy as a tradeoff between energy yield and protein cost. *Proc Natl Acad Sci U S A* 110:10039–10044. <https://doi.org/10.1073/pnas.1215283110>.
- Contin M, Corcimaru S, De Nobili M, Brookes PC. 2000. Temperature changes and the ATP concentration of the soil microbial biomass. *Soil Biol Biochem* 32:1219–1225. [https://doi.org/10.1016/S0038-0717\(00\)00038-9](https://doi.org/10.1016/S0038-0717(00)00038-9).
- Steinweg JM, Plante AF, Conant RT, Paul EA, Tanaka DL. 2008. Patterns of substrate utilization during long-term incubations at different temperatures. *Soil Biol Biochem* 40:2722–2728. <https://doi.org/10.1016/j.soilbio.2008.07.002>.
- Pold G, Domeignoz-Horta LA, Morrison EW, Frey SD, Sistla SA, DeAngelis KM. 2020. Carbon use efficiency and its temperature sensitivity covary in soil bacteria. *mBio* 11:e02293-19. <https://doi.org/10.1128/mBio.02293-19>.
- Raymond-Bouchard I, Whyte LG. 2017. From transcriptomes to metatranscriptomes: cold adaptation and active metabolisms of psychrophiles from cold environments, p 437–457. *In* Margesin R (ed), *Psychrophiles: from biodiversity to biotechnology*. Springer International Publishing, Cham, Switzerland.
- Hébraud M, Potier P. 1999. Cold shock response and low temperature adaptation in psychrotrophic bacteria. *J Mol Microbiol Biotechnol* 1:211–219.
- Raymond-Bouchard I, Tremblay J, Altshuler I, Greer CW, Whyte LG. 2018. Comparative transcriptomics of cold growth and adaptive features of a eury- and steno-psychrophiles. *Front Microbiol* 9:1565. <https://doi.org/10.3389/fmicb.2018.01565>.
- Wang F, Xiao X, Ou H-Y, Gai Y, Wang F. 2009. Role and regulation of fatty acid biosynthesis in the response of *Shewanella piezotolerans* WP3 to different temperatures and pressures. *J Bacteriol* 191:2574–2584. <https://doi.org/10.1128/JB.00498-08>.
- Ting L, Williams TJ, Cowley MJ, Lauro FM, Guilhaus M, Raftery MJ, Cavicchioli R. 2010. Cold adaptation in the marine bacterium, *Sphingopyxis alaskensis*, assessed using quantitative proteomics. *Environ Microbiol* 12:2658–2676. <https://doi.org/10.1111/j.1462-2920.2010.02235.x>.
- Piette F, D'Amico S, Mazzucchelli G, Danchin A, Leprince P, Feller G. 2011. Life in the cold: a proteomic study of cold-repressed proteins in the Antarctic bacterium *Pseudoalteromonas haloplanktis* TAC125. *Appl Environ Microbiol* 77:3881–3883. <https://doi.org/10.1128/AEM.02757-10>.

27. De Maayer P, Anderson D, Cary C, Cowan DA. 2014. Some like it cold: understanding the survival strategies of psychrophiles. *EMBO Rep* 15:508–517. <https://doi.org/10.1002/embr.201338170>.
28. McCallum KL, Heikkila JJ, Inniss WE. 1986. Temperature-dependent pattern of heat shock protein synthesis in psychrophilic and psychrotrophic microorganisms. *Can J Microbiol* 32:516–521. <https://doi.org/10.1139/m86-094>.
29. Hakeda Y, Fukunaga N. 1983. Effect of temperature stress on adenylate pools and energy charge in a psychrophilic bacterium, *Vibrio* sp. ABE-1. *Plant Cell Physiol* 24:849–856. <https://doi.org/10.1093/oxfordjournals.pcp.a076586>.
30. Napolitano MJ, Shain DH. 2005. Distinctions in adenylate metabolism among organisms inhabiting temperature extremes. *Extremophiles* 9: 93–98. <https://doi.org/10.1007/s00792-004-0424-1>.
31. Wang F, Wang P, Chen M, Xiao X. 2004. Isolation of extremophiles with the detection and retrieval of *Shewanella* strains in deep-sea sediments from the west Pacific. *Extremophiles* 8:165–168. <https://doi.org/10.1007/s00792-003-0365-0>.
32. Xiao X, Wang P, Zeng X, Bartlett DH, Wang F. 2007. *Shewanella psychrophila* sp. nov. and *Shewanella piezotolerans* sp. nov., isolated from west Pacific deep-sea sediment. *Int J Syst Evol Microbiol* 57:60–65. <https://doi.org/10.1099/ijs.0.64500-0>.
33. Dufault-Thompson K, Jian H, Cheng R, Li J, Wang F, Zhang Y. 2017. A genome-scale model of *Shewanella piezotolerans* simulates mechanisms of metabolic diversity and energy conservation. *mSystems* 2:e00165-16. <https://doi.org/10.1128/mSystems.00165-16>.
34. Xu Z, Guo J, Yue Y, Meng J, Sun X. 2018. *In silico* genome-scale reconstruction and analysis of the *Shewanella loihica* PV-4 metabolic network. *J Biol Syst* 26:373–397. <https://doi.org/10.1142/S0218339018500171>.
35. Tang X, Yu L, Yi Y, Wang J, Wang S, Meng C, Liu S, Hao Y, Zhang Y, Cao X, Jian H, Xiao X. 2021. Phylogenomic analysis reveals a two-stage process of the evolutionary transition of *Shewanella* from the upper ocean to the hadal zone. *Environ Microbiol* 23:744–756. <https://doi.org/10.1111/1462-2920.15162>.
36. Xu G, Jian H, Xiao X, Wang F. 2017. Complete genome sequence of *Shewanella psychrophila* WP2, a deep-sea bacterium isolated from west Pacific sediment. *Mar Genomics* 35:19–21. <https://doi.org/10.1016/j.margen.2017.03.004>.
37. Dahal S, Poudel S, Thompson RA. 2017. Genome-scale modeling of thermophilic microorganisms. *Adv Biochem Eng Biotechnol* 160:103–119. [https://doi.org/10.1007/10\\_2016\\_45](https://doi.org/10.1007/10_2016_45).
38. Fondi M, Maida I, Perrin E, Mellerà A, Mocali S, Parrilli E, Tutino ML, Liò P, Fani R. 2015. Genome-scale metabolic reconstruction and constraint-based modelling of the Antarctic bacterium *Pseudoalteromonas haloplanktis* TAC 125. *Environ Microbiol* 17:751–766. <https://doi.org/10.1111/1462-2920.12513>.
39. Ates O, Oner ET, Arga KY. 2011. Genome-scale reconstruction of metabolic network for a halophilic extremophile, *Chromohalobacter salexigens* DSM 3043. *BMC Syst Biol* 5:12. <https://doi.org/10.1186/1752-0509-5-12>.
40. Varma A, Palsson BO. 1994. Stoichiometric flux balance models quantitatively predict growth and metabolic by-product secretion in wild-type *Escherichia coli* W3110. *Appl Environ Microbiol* 60:3724–3731. <https://doi.org/10.1128/aem.60.10.3724-3731.1994>.
41. Edwards JS, Palsson BO. 2000. Metabolic flux balance analysis and the *in silico* analysis of *Escherichia coli* K-12 gene deletions. *BMC Bioinformatics* 1:1. <https://doi.org/10.1186/1471-2105-1-1>.
42. Chang RL, Andrews K, Kim D, Li Z, Godzik A, Palsson BO. 2013. Structural systems biology evaluation of metabolic thermotolerance in *Escherichia coli*. *Science* 340:1220–1223. <https://doi.org/10.1126/science.1234012>.
43. Henry CS, Broadbelt LJ, Hatzimanikatis V. 2007. Thermodynamics-based metabolic flux analysis. *Biophys J* 92:1792–1805. <https://doi.org/10.1529/biophysj.106.093138>.
44. Hamilton JJ, Dwivedi V, Reed JL. 2013. Quantitative assessment of thermodynamic constraints on the solution space of genome-scale metabolic models. *Biophys J* 105:512–522. <https://doi.org/10.1016/j.bpj.2013.06.011>.
45. Fabiano B, Perego P. 2002. Thermodynamic study and optimization of hydrogen production by *Enterobacter aerogenes*. *Int J Hydrogen Energy* 27:149–156. [https://doi.org/10.1016/S0360-3199\(01\)00102-1](https://doi.org/10.1016/S0360-3199(01)00102-1).
46. Amend JP, Shock EL. 1998. Energetics of amino acid synthesis in hydrothermal ecosystems. *Science* 281:1659–1662. <https://doi.org/10.1126/science.281.5383.1659>.
47. Noor E, Bar-Even A, Flamholz A, Reznik E, Liebermeister W, Milo R. 2014. Pathway thermodynamics highlights kinetic obstacles in central metabolism. *PLoS Comput Biol* 10:e1003483. <https://doi.org/10.1371/journal.pcbi.1003483>.
48. Lieven C, Beber ME, Olivier BG, Bergmann FT, Ataman M, Babaei P, Bartell JA, Blank LM, Chauhan S, Correia K, Diener C, Dräger A, Ebert BE, Edirisinghe JN, Faria JP, Feist AM, Fengos G, Fleming RMT, García-Jiménez B, Hatzimanikatis V, van Helvoirt W, Henry CS, Hermjakob H, Herrgård MJ, Kaafarani A, Kim HU, King Z, Klamt S, Klipp E, Koehorst JJ, König M, Lakshmanan M, Lee D-Y, Lee SY, Lee S, Lewis NE, Liu F, Ma H, Machado D, Mahadevan R, Maia P, Mardinoglu A, Medlock GL, Monk JM, Nielsen J, Nielsen LK, Nogales J, Nookaew I, Palsson BO, Papin JA, et al. 2020. MEM-OTE for standardized genome-scale metabolic model testing. *Nat Biotechnol* 38:272–276. <https://doi.org/10.1038/s41587-020-0446-y>.
49. Saifuddin M, Bhatnagar JM, Segrè D, Finzi AC. 2019. Microbial carbon use efficiency predicted from genome-scale metabolic models. *Nat Commun* 10:3568. <https://doi.org/10.1038/s41467-019-11488-z>.
50. Jørgensen BB, Boetius A. 2007. Feast and famine — microbial life in the deep-sea bed. *Nat Rev Microbiol* 5:770–781. <https://doi.org/10.1038/nrmicro1745>.
51. Schippers A, Neretin LN, Kallmeyer J, Ferdelman TG, Cragg BA, Parkes RJ, Jørgensen BB. 2005. Prokaryotic cells of the deep sub-seafloor biosphere identified as living bacteria. *Nature* 433:861–864. <https://doi.org/10.1038/nature03302>.
52. Mao J, Blanchard AE, Lu T. 2015. Slow and steady wins the race: a bacterial exploitative competition strategy in fluctuating environments. *ACS Synth Biol* 4:240–248. <https://doi.org/10.1021/sb4002008>.
53. Koch AL. 1997. Microbial physiology and ecology of slow growth. *Microbiol Mol Biol Rev* 61:3. <https://doi.org/10.1128/mmlbr.61.3.305-318.1997>.
54. Gray DA, Dugar G, Gamba P, Strahl H, Jonker MJ, Hamoen LW. 2019. Extreme slow growth as alternative strategy to survive deep starvation in bacteria. *Nat Commun* 10:890. <https://doi.org/10.1038/s41467-019-08719-8>.
55. San Román M, Cancela H, Acerenza L. 2014. Source and regulation of flux variability in *Escherichia coli*. *BMC Syst Biol* 8:67. <https://doi.org/10.1186/1752-0509-8-67>.
56. Koh HY, Park H, Lee JH, Han SJ, Sohn YC, Lee SG. 2017. Proteomic and transcriptomic investigations on cold-responsive properties of the psychrophilic Antarctic bacterium *Psychrobacter* sp. PAMC 21119 at subzero temperatures. *Environ Microbiol* 19:628–644. <https://doi.org/10.1111/1462-2920.13578>.
57. Stettner AI, Segrè D. 2013. The cost of efficiency in energy metabolism. *Proc Natl Acad Sci U S A* 110:9629–9630. <https://doi.org/10.1073/pnas.1307485110>.
58. Chen X, Schreiber K, Appel J, Makowka A, Fähnrich B, Roettger M, Hajirezaei MR, Sönnichsen FD, Schönheit P, Martin WF, Gutekunst K. 2016. The Entner–Doudoroff pathway is an overlooked glycolytic route in cyanobacteria and plants. *Proc Natl Acad Sci U S A* 113:5441–5446. <https://doi.org/10.1073/pnas.1521916113>.
59. Czajka JJ, Abernathy MH, Benites VT, Baidoo EEK, Deming JW, Tang YJ. 2018. Model metabolic strategy for heterotrophic bacteria in the cold ocean based on *Colwellia psychrethraea* 34H. *Proc Natl Acad Sci U S A* 115:12507–12512. <https://doi.org/10.1073/pnas.1807804115>.
60. Crousilles A, Dolan SK, Brear P, Chirgadze DY, Welch M. 2018. Gluconeogenic precursor availability regulates flux through the glyoxylate shunt in *Pseudomonas aeruginosa*. *J Biol Chem* 293:14260–14269. <https://doi.org/10.1074/jbc.RA118.004514>.
61. Yano T, Yoshida N, Yu F, Wakamatsu M, Takagi H. 2015. The glyoxylate shunt is essential for CO<sub>2</sub>-requiring oligotrophic growth of *Rhodococcus erythropolis* N9T-4. *Appl Microbiol Biotechnol* 99:5627–5637. <https://doi.org/10.1007/s00253-015-6500-x>.
62. Koedooder C, Guéneuguès A, Van Geersdaële R, Vergé V, Bouquet F-Y, Labreuche Y, Obernosterer I, Blain S. 2018. The role of the glyoxylate shunt in the acclimation to iron limitation in marine heterotrophic bacteria. *Front Mar Sci* 5:435. <https://doi.org/10.3389/fmars.2018.00435>.
63. Hunt KA, Flynn JM, Naranjo B, Shikhare ID, Gralnick JA. 2010. Substrate-level phosphorylation is the primary source of energy conservation during anaerobic respiration of *Shewanella oneidensis* strain MR-1. *J Bacteriol* 192:3345–3351. <https://doi.org/10.1128/JB.00090-10>.
64. Napolitano MJ, Shain DH. 2004. Four kingdoms on glacier ice: convergent energetic processes boost energy levels as temperatures fall. *Proc Biol Sci* 271(Suppl 5):S273–S276. <https://doi.org/10.1098/rsbl.2004.0180>.
65. Pinchuk GE, Hill EA, Geydebrekht OV, De Ingeniis J, Zhang X, Osterman A, Scott JH, Reed SB, Romine MF, Konopka AE, Beliaev AS, Fredrickson JK, Reed JL. 2010. Constraint-based model of *Shewanella oneidensis* MR-1 metabolism: a tool for data analysis and hypothesis generation. *PLoS Comput Biol* 6:e1000822. <https://doi.org/10.1371/journal.pcbi.1000822>.
66. Bushnell B. 2014. BBMap: a fast, accurate, splice-aware aligner. Lawrence Berkeley National Lab, Berkeley, CA.

67. Liao Y, Smyth GK, Shi W. 2014. featureCounts: an efficient general purpose program for assigning sequence reads to genomic features. *Bioinformatics* 30:923–930. <https://doi.org/10.1093/bioinformatics/btt656>.
68. Love MI, Huber W, Anders S. 2014. Moderated estimation of fold change and dispersion for RNA-seq data with DESeq2. *Genome Biol* 15:550. <https://doi.org/10.1186/s13059-014-0550-8>.
69. Zhang Y, Sievert SM. 2014. Pan-genome analyses identify lineage- and niche-specific markers of evolution and adaptation in *Epsilonproteobacteria*. *Front Microbiol* 5:110. <https://doi.org/10.3389/fmicb.2014.00110>.
70. Steffensen JL, Dufault-Thompson K, Zhang Y. 2016. PSAMM: a portable system for the analysis of metabolic models. *PLoS Comput Biol* 12:e1004732. <https://doi.org/10.1371/journal.pcbi.1004732>.
71. Ong WK, Vu TT, Lovendahl KN, Lull JM, Serres MH, Romine MF, Reed JL. 2014. Comparisons of *Shewanella* strains based on genome annotations, modeling, and experiments. *BMC Syst Biol* 8:31. <https://doi.org/10.1186/1752-0509-8-31>.
72. Cantalapiedra CP, Hernández-Plaza A, Letunic I, Bork P, Huerta-Cepas J. 2021. eggNOG-mapper v2: functional annotation, orthology assignments, and domain prediction at the metagenomic scale. *Mol Biol Evol* 38:5825–5829. <https://doi.org/10.1093/molbev/msab293>.
73. Huerta-Cepas J, Forslund K, Coelho LP, Szklarczyk D, Jensen LJ, von Mering C, Bork P. 2017. Fast genome-wide functional annotation through orthology assignment by eggNOG-Mapper. *Mol Biol Evol* 34:2115–2122. <https://doi.org/10.1093/molbev/msx148>.
74. Huerta-Cepas J, Szklarczyk D, Heller D, Hernández-Plaza A, Forslund SK, Cook H, Mende DR, Letunic I, Rattei T, Jensen LJ, von Mering C, Bork P. 2019. eggNOG 5.0: a hierarchical, functionally and phylogenetically annotated orthology resource based on 5090 organisms and 2502 viruses. *Nucleic Acids Res* 47:D309–D314. <https://doi.org/10.1093/nar/gky1085>.
75. Kanehisa M, Goto S. 2000. KEGG: Kyoto Encyclopedia of Genes and Genomes. *Nucleic Acids Res* 28:27–30. <https://doi.org/10.1093/nar/28.1.27>.
76. Tatusov RL, Galperin MY, Natale DA, Koonin EV. 2000. The COG database: a tool for genome-scale analysis of protein functions and evolution. *Nucleic Acids Res* 28:33–36. <https://doi.org/10.1093/nar/28.1.33>.
77. Orth JD, Conrad TM, Na J, Lerman JA, Nam H, Feist AM, Palsson BØ. 2011. A comprehensive genome-scale reconstruction of *Escherichia coli* metabolism—2011. *Mol Syst Biol* 7:535. <https://doi.org/10.1038/msb.2011.65>.
78. Thiele I, Vlassis N, Fleming RMT. 2014. fastGapFill: efficient gap filling in metabolic networks. *Bioinformatics* 30:2529–2531. <https://doi.org/10.1093/bioinformatics/btu321>.
79. Satish Kumar V, Dasika MS, Maranas CD. 2007. Optimization based automated curation of metabolic reconstructions. *BMC Bioinformatics* 8:212. <https://doi.org/10.1186/1471-2105-8-212>.
80. King ZA, Lu J, Dräger A, Miller P, Federowicz S, Lerman JA, Ebrahim A, Palsson BO, Lewis NE. 2016. BiGG Models: a platform for integrating, standardizing and sharing genome-scale models. *Nucleic Acids Res* 44:D515–D522. <https://doi.org/10.1093/nar/gkv1049>.
81. Du B, Zhang Z, Grubner S, Yurkovich JT, Palsson BO, Zielinski DC. 2018. Temperature-dependent estimation of Gibbs energies using an updated group-contribution method. *Biophys J* 114:2691–2702. <https://doi.org/10.1016/j.bpj.2018.04.030>.
82. Goldberg RN, Tewari YB, Bhat TN. 2004. Thermodynamics of enzyme-catalyzed reactions—a database for quantitative biochemistry. *Bioinformatics* 20:2874–2877. <https://doi.org/10.1093/bioinformatics/bth314>.
83. Kim S, Thiessen PA, Bolton EE, Chen J, Fu G, Gindulyte A, Han L, He J, He S, Shoemaker BA, Wang J, Yu B, Zhang J, Bryant SH. 2016. PubChem substance and compound databases. *Nucleic Acids Res* 44:D1202–13. <https://doi.org/10.1093/nar/gkv951>.
84. Albe KR, Butler MH, Wright BE. 1990. Cellular concentrations of enzymes and their substrates. *J Theor Biol* 143:163–195. [https://doi.org/10.1016/s0022-5193\(05\)80266-8](https://doi.org/10.1016/s0022-5193(05)80266-8).
85. Rea LM, Parker RA. 2014. Designing and conducting survey research: a comprehensive guide. John Wiley & Sons, Hoboken, NJ.